

Fine Scale Imaging of Structure at and Near the Mantle  
Transition Zone Using a Generalized Radon Transform

by

Rosalee Alicia Lamm

B.S. Geophysics–Math  
Brown University, 2003

SUBMITTED TO THE DEPARTMENT OF EARTH, ATMOSPHERIC AND  
PLANETARY SCIENCES IN PARTIAL FULFILLMENT OF THE  
REQUIREMENTS FOR THE DEGREE OF

MASTER OF SCIENCE IN EARTH, ATMOSPHERIC AND PLANETARY  
SCIENCES

AT THE  
MASSACHUSETTS INSTITUTE OF TECHNOLOGY

JUNE 2006

© 2006 Massachusetts Institute of Technology  
All rights reserved.

Signature of Author: \_\_\_\_\_

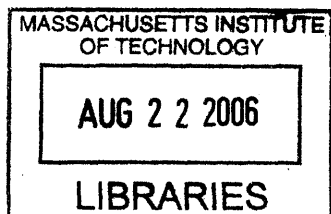
Department of Earth, Atmospheric and Planetary Sciences  
May 12, 2006

Certified by: \_\_\_\_\_

Robert van der Hilst  
Cecil and Ida Green Professor of Earth and Planetary Sciences  
Thesis Supervisor

Accepted by: \_\_\_\_\_

Maria Zuber  
E.A. Griswold Professor of Geophysics  
Head, Department of Earth, Atmospheric and Planetary Sciences



ARCHIVED



# Fine Scale Imaging of Structure at and Near the Mantle Transition Zone Using a Generalized Radon Transform

by  
Rosalee Alicia Lamm

Submitted to the Department of Earth, Atmospheric and Planetary Sciences  
on May 12, 2006 in Partial Fulfillment of the Requirements for the Degree  
of Master of Science in Earth, Atmospheric and Planetary Sciences.

## ABSTRACT

We apply a generalized Radon transform (GRT) to the study of the transition zone discontinuities. The transition zone discontinuities, e.g. the '410' and '660', result from mineral phase changes that occur at depths constrained by temperature and chemistry, and can provide information about the conditions of the mantle within the transition zone. Previous global studies of topography on the transition zone discontinuities use *SS* data and are limited by the low lateral resolution provided by *SS* waves, on the order of about 1000 kilometers. The GRT employs inverse scattering theory to image perturbations in mass density and elastic parameters of a medium, and can resolve structure on the order of 100 kilometers; the limit of this resolution has yet to be tested. This study maps discontinuity depths in the northwest Pacific Ocean with a lateral spatial sampling of 1° and a vertical sampling of five kilometers. We observe striking variations in the depth, strength, and continuity of the '410', '520', and '660' seismic discontinuities, as well as the presence of structure beyond the bounds of what is traditionally considered to be the transition zone. Topographies on the '410' and '660' are alternately positively and negatively correlated, suggesting that both composition and temperature contribute to the observed depths. Preliminary analysis of '410' depths, which assumes no variations in chemistry, yields an upper bound for temperature variations of  $\pm 280\text{K}$ . Future tests and data preprocessing should further improve the GRT results.

Thesis Supervisor: Robert van der Hilst

Title: Cecil and Ida Green Professor of Earth and Planetary Sciences



## CONTENTS

<b>1. Background and motivation</b>	7
<b>2. Methodology</b>	10
2.1. <i>Notation and scattering geometry</i>	10
2.2. <i>Isochrons and map de-migration</i>	12
2.3. <i>The GRT inversion</i>	
2.4. <i>Application of the GRT to SdS data</i>	14
<b>3. Data Selection and Preprocessing</b>	15
<b>4. Synthetic tests</b>	18
<b>5. Results</b>	21
<b>6. Discussion</b>	28
<b>7. Conclusion</b>	31
<b>Tables</b>	33
<b>References</b>	34

## LIST OF FIGURES

Figure 1. $S_{660}S$ ray paths .....	9
Figure 2. Geometry of the GRT .....	11
Figure 3. Distribution of bounce points, sources and receivers for $SS$ data.....	16
Figure 4. Record section showing $SS$ and its precursors .....	17
Figure 5. GRT on synthetics with a Hilbert transform .....	19
Figure 6. GRT on synthetics, without a Hilbert transform .....	19
Figure 7. Dependence of the GRT on the number of data used .....	21
Figure 8. GRT image gathers before and after integration over scattering angle.....	22
Figure 9. Locations of the cross-sections in figure 10.....	23
Figure 10. Cross-sections made by plotting adjacent vertical profiles .....	24
Figure 11. Comparison between data and synthetics results .....	25
Figure 12. Thickness and topography variation and correlation .....	27

## 1. Background and motivation

Two major mantle discontinuities at globally average depths of 410 and 660 kilometers mark the boundary between the upper and lower mantle and delineate the mantle transition zone. These discontinuities, referred to as the '410' and '660', are caused by the  $\alpha$ - to  $\beta$ -spinel and the post-spinel ( $\gamma$ -spinel to perovskite and magnesiowüstite) phase changes, respectively. As such, their depths primarily reflect the pressures needed for the phase changes to occur, which are determined by thermodynamic parameters. Thus, the depth to the discontinuities is controlled by, and indicative of, the temperature and composition of the mantle in which it lies. This leads one to imagine that the seismic observations of the depth and character of the '410' and '660' could be used to find mantle temperature and composition, provided that the thermal and compositional conditions that can produce seismic observations are known, e.g. from mineral physics research. If an accurate inversion is truly possible, depth estimates of the '410' and '660' could act as a thermal and chemical probe, helping to further our understanding of mantle convection.

The Clapeyron slope describes the temperature dependence of the transition pressure of a phase change. The Clapeyron slopes in the pure magnesium system of the  $\alpha$ - $\beta$  and the post-spinel transformations are under some debate, but most values are around +3 MPa/K for the former, and -2 MPa/K for the latter (*Fei et al.*, 2004; *Irfune et al.*, 1998). Strictly speaking, the Clapeyron slope is not defined in a multi-component system, since changes occur over a pressure range, while the Clapeyron slope defines a single transition pressure. However, seismic studies commonly assume the same Clapeyron slope for an iron bearing system, e.g. the mantle, as for the pure magnesium system. This is not a bad approximation, since seismic waves “see” the region over which the transformation occurs more or less as a discontinuity. *Lebedev et al.* (2002a) performed a study in which the thickness and velocity of the transition zone were calculated, and from this the seismic Clapeyron slope inferred. About 2 and -3 MPa/K, their values agree with mineral physics estimates of the  $\alpha$ - $\beta$  and the post-spinel Clapeyron slopes, respectively.

Though the transition zone discontinuities are approximated as sharp seismic discontinuities, consideration of the two-phase region itself can yield valuable information. Like the depth, the width of this region and the change in the percentage of

each phase are controlled by the temperature of the mantle and the chemistry of the two phases. The conditions of the mantle are thus best constrained by considering not only the depth of the phase changes, but also the width and shape of the two-phase region.

Estimations of the thickness of the transition zone (between the '410' and the '660') are fairly consistent. Deviations from the average value of 250 km range from  $\pm 10$  km to  $\pm 30$  km (*Bock et al.*, 1995; *Chevrot et al.*, 1999; *Gu et al.*, 1998; *Gu and Dziewonski*, 2002; *Lebedev et al.*, 2002a; *Li et al.*, 2002). Global average depths of 410 and 660 are generally consistent.

The extensive research of the TZ discontinuities over the past few decades has answered many questions, but several first order issues remain controversial. For example, why is topography on the '410' and '660' not observed to be anti-correlated, with larger variations on the '410' than the '660', as expected from the Clapeyron slopes of the associated phase transformations (*Bina and Helffrich*, 1994; *Bock et al.*, 1995; *Gu et al.*, 1998; *Flanagan and Shearer*, 1998a)? Are thermal anomalies at the '410' independent of those at the '660', or is the scale of the lateral variations in topography too small to be detected (for instance, subducting slabs crossing the '410' would affect topography over a lateral region of only about 100 kilometers, measured parallel to the slab dip)? A mid-TZ discontinuity resulting from the  $\beta$ - to  $\gamma$ -spinel phase transformation is predicted by mineral physics. A discontinuity at about 520 km, possibly corresponding to this phase change, can sometimes be detected, but observations of the '520' are spotty. Does the '520' result from the  $\beta$ - to  $\gamma$ -spinel transformation, or could transitions in the pyroxene ( $\text{MgSiO}_3$ ) system contribute to the signal? Does the varying strength and visibility of the '520' result from changes in composition and temperature (e.g. *Gu et al.*, 1998; *Deuss and Woodhouse*, 2001), or is the '520' simply a very weak arrival that is easily masked by noise (e.g. *Flanagan and Shearer*, 1998)? Are there other interfaces that can be detected by seismic methods, and if so, what do they represent? Some studies show seismic evidence of phase changes in the  $\text{MgSiO}_3$  system (*Simmons and Gurrola*, 2000; *Castillo et al.*, 2001), but this interpretation is widely contested. Lastly, what is the shape of the velocity or density profile across the transition zone discontinuities, and do they agree with mineral physics predictions? *Melbourne and Helmberger* (1998) and *Xu et al.* (2003) suggest that the '410' km velocity profile is non-linear, with a sharp discontinuity toward the bottom, which agrees roughly with mineral physics (e.g.



*Stixrude, 1997; Irifune and Isshiki, 1998*), but this may change with varying mantle chemistry. The '660' seems sharp enough that the change in velocity with increasing depth across the interface is regarded seismically as a discontinuous step (e.g. *Castle and Creager, 2000; Xu et al., 2003*). Further characterization of the observed and predicted elastic properties across the seismic discontinuities (the two phase region), as well as reliable, high-resolution imaging, should help to clear up these questions.

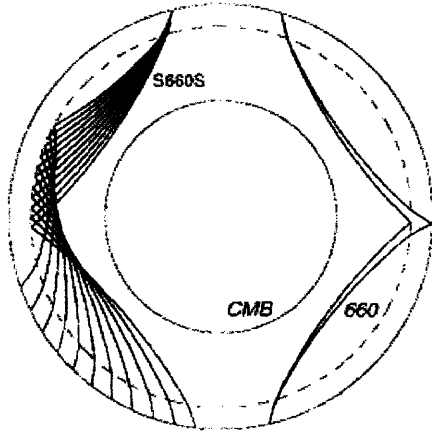


Figure 1.  $S_{660}S$  ray paths. Paths on the right illustrate ray paths for waves emanating from a single source.  $SS$  and  $S_{410}S$  travel similar paths but reflect from the surface and 410 km depth, respectively. Because  $S_{660}S$  and  $S_{410}S$  reflect from deeper interfaces than  $SS$ , they travel less distance and arrive before the  $SS$  phase.

Various methods have been used to study the mid-mantle discontinuities.  $SS$  precursors ( $SS$  waves that reflect from the underside of the mantle discontinuities; see figure 1) are commonly used because of the global data coverage they afford. However, imaging the topography of mantle discontinuities with these kind of data may introduce gross errors into the interpretation (*Neele et al., 1997; Chaljub and Tarantola, 1997; Zhao and Chevrot, 2003*).  $SS$  (or  $PP$ ) precursors can resolve the depth and shape of deflections for very large lateral variations only, on the order of 1000 km, due to the size of their sensitivity kernels. These kernels describe an area from which reflected energy arrives at a given receiver within a small enough time window to constructively interfere. Since this window is defined by the wavelength of the waves, the wavelength determines the size of the sensitivity kernel. Studies that use ray theory effectively average the topography within the region sampled by the kernel. The resulting depth estimate can be used to describe topography with lateral variations on the order of the size of the kernel, but detection of smaller lateral variations requires the use of 3D scattering theory.

Alternatively,  $Pds$  waves (upgoing  $P$  waves that convert to  $S$  waves at the interface) can be used. These are able to resolve variations on length scales of an order of

magnitude smaller than *SS* waves (*Chevrot et al.*, 1999); however, since the conversion takes place almost directly beneath the receiver, data coverage is limited to areas where stations are located.

Owing to its use of scattering theory, the generalized Radon transform is able to image fine-scale structure using *SS* precursors, without introducing gross errors in topography. Ideally, the GRT does not rely on the accuracy of the background model, because it is able to estimate the error in the background model assumed and to apply corrections accordingly. Practically, however, it may not be possible to determine the error without more vigorous statistical estimation (e.g. *Ma et al.*, in preparation). The GRT is then equally reliant on the accuracy of the velocity model as are *Pds* and *SS* studies; in its most basic form, the advantage of the GRT then rests on its ability to image structure on the scale found in *Pds* studies, but with the global coverage provided by *SS* data.

The GRT is currently being used to study the core-mantle boundary using *ScS* and *SKKS* ray paths (*Wang et al.*, under review). The present study builds on the work of *Wang et al.* by developing the generalized Radon transform for use with *SS* data. We test the robustness of the GRT on synthetic seismograms that include *SS*, *S<sub>410S</sub>*, and *S<sub>660S</sub>* waveforms. We then apply the GRT to real *SS* data that sample a small region in the northwest Pacific Ocean, with the objective of detecting and characterizing interfaces at depth. The work presented here focuses on detecting discontinuities; future work will address the shape of the discontinuities. Ultimately, our goal is to map variations in the temperature and composition of the mantle, information that will further our understanding of mantle convection and evolution.

## 2. Methodology

The GRT is a method of map migration that uses the scattered wavefield to image a single scattering point. The development of the GRT inversion is presented below, following that of *Wang, et al.* (under review), after which we discuss the specific form of the GRT used for this research.

### 2.1 Notation and scattering geometry

The geometry for the GRT is shown in figure 2. The GRT uses hundreds to

thousands of waveform data from sources and receivers around the globe. In the notation of the GRT,  $s$  signifies a relation to the source, and  $r$  a relation to the receiver. Thus,  $\mathbf{x}^s$  is the location of the source,  $\mathbf{x}^r$  the location of the receiver. The receivers record the three components of the data, the vertical, radial, and transverse displacement, denoted by  $u_p$ , with  $p=1,2,3$ . Each data point can be uniquely defined by the source, receiver, and the time since the earthquake, i.e.  $u_p = u_p(\mathbf{x}^s, \mathbf{x}^r, t)$ .

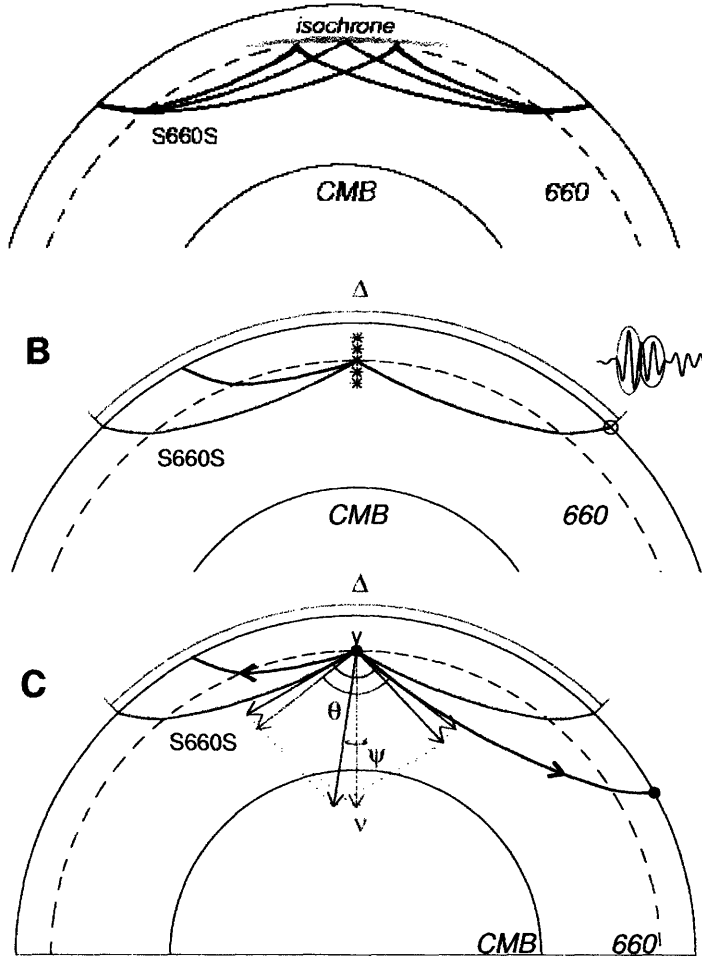


Figure 2. Geometry of the GRT. (A) Illustration of an isochron, from which all reflections arrive at the same time. (B) Specular (red) and non-specular (blue) ray paths for a single scattering point. Because  $SS$  is a mini-max time path, waves that travel non-specular paths may arrive before or after the specular ray. In this figure the specular wave arrives first. Ray theory uses only specular data (red circle on waveform at right); the GRT utilizes scattered energy as well (blue circle). (C) GRT geometry for both specular (red) and non-specular (blue) paths. Unmarked arrows represent slowness vectors  $\mathbf{p}^r$  and  $\mathbf{p}^s$  at  $y$ .  $\theta$  denotes the angle between  $\mathbf{p}^r(y)$  and  $\mathbf{p}^s(y)$ . The migration dip,  $\nu$ , is the normalized sum of  $\mathbf{p}^r(y)$  and  $\mathbf{p}^s(y)$ , and describes the isochron normal at  $y$ .  $\psi$ , the scattering azimuth, describes the angle between a geographic reference and the projection of  $\nu$  onto the surface.

The slowness of the path from the source or receiver to the image point  $y$ , evaluated at  $y$ , is  $\mathbf{p}^r(y)$  or  $\mathbf{p}^s(y)$ , while  $\mathbf{p}^r(\mathbf{x}^r)$  or  $\mathbf{p}^s(\mathbf{x}^s)$  is the slowness evaluated at the receiver or source. The projection of  $\mathbf{p}(\mathbf{x})$  onto the horizontal plane gives  $\pi(\mathbf{x})$ , the horizontal slowness, which is constant over the ray path from the surface to the image point, and can be determined by the geometry of the source-receiver pairs. The remaining variables used in the GRT are derived from the slowness vector,  $\mathbf{p}$ . The

migration dip  $\nu^m$  is given by  $\mathbf{p}^m/|\mathbf{p}^m|$  where  $\mathbf{p}^m = \mathbf{p}^s(\mathbf{y}) + \mathbf{p}^r(\mathbf{y})$ . The migration dip describes the asymmetry of the path, as well as the resolution of the image gather; this is discussed below.

The scattering vector  $\boldsymbol{\psi}$  is related to the slowness through the wavenumber  $\mathbf{k}$ :  $\boldsymbol{\psi} = (\mathbf{k}^s \times \mathbf{k}^r) \times \mathbf{v}^m$ . From  $\boldsymbol{\psi}$ , two essential parameters are derived:  $\theta$  and  $\psi$ .  $\theta$  is the scattering angle, the angle between  $\mathbf{p}^r(\mathbf{y})$  and  $\mathbf{p}^s(\mathbf{y})$ , where  $\sin(\theta) = |\boldsymbol{\psi}|$ . The scattering azimuth  $\psi$  describes the angle between  $\boldsymbol{\psi}$  (the projection of  $\mathbf{p}^m$  onto the surface) and a geographic reference, e.g. north.

The geometry at the scattering point  $\mathbf{y}$  gives rise to the weight  $|\mathbf{p}^m|^3$ . To see this, consider a geometry in which  $\mathbf{p}^m$  is large compared to other possibilities for  $\mathbf{p}^m$  at the given scattering point. For  $\mathbf{p}^m$  large,  $\theta$  must be small. Likewise, for small  $\mathbf{p}^m$ ,  $\theta$  must be large. Thus for large  $\mathbf{p}^m$  the reflection is near vertical, while for small  $\mathbf{p}^m$  the ray becomes parallel to the interface. This gives rise to a dependence of the vertical resolution on  $\mathbf{p}^m$ , since the depth of a reflector can be most precisely determined for vertical reflections. The difference in the distance traveled for reflections from adjacent image points in a vertical profile is approximately twice the vertical separation between the two points, yielding a travel time difference  $dt = 2 \times \mathbf{p} \times dz$ . Simple geometry shows that the difference in the distance traveled for small  $\mathbf{p}^m$  is given by  $ds = 2 \times dz \times \cos(\theta/2)$ ; thus,  $ds$  and  $dt$  are a factor of  $\cos(\theta/2)$  smaller than for large  $\mathbf{p}^m$ . Because of the resolution dependence on  $\mathbf{p}^m$ , larger values of  $\mathbf{p}^m$  are weighted more heavily. Poor spatial resolution also causes a vertical dilation of the GRT image with decreasing  $\mathbf{p}^m$  (i.e. increasing  $\theta$ ).

## 2.2 Isochrons and map de-migration

For a given source and receiver, the location of the point that causes scattered energy in the waveform data is not uniquely resolved by the travel time. The locations of the possible scattering points that could cause an arrival at a given time lie along a hyperbolic curve, called an isochron (figure 2-A). Translating the arrival time to scattering location results in smearing the energy over the surface of the isochron. For this reason, it is necessary to “migrate” the resulting hyperbolic image to the correct scattering point location.

In order to resolve the location of a scattering point, the GRT images a point at the

intersection of several isochrons. More precisely, the GRT integrates the data over all isochrons at a specific point. In the notation given above, for a point  $y$ ,  $u(\mathbf{x}^s, \mathbf{x}', y)$  is calculated for all  $\mathbf{x}^s$  and  $\mathbf{x}'$ , and is integrated over  $\mathbf{v}^m$ , the unit vector of  $\mathbf{p}^m$ .  $\mathbf{p}^m$  is normal to the isochron; integration over  $\mathbf{v}^m$  at  $y$  denotes integration over all isochrons represented in the data coverage that pass through  $y$ .

### 2.3 The GRT inversion

The forward problem can be described simply in the following way:

$$u = F * \delta c \quad (1)$$

where  $u$  is the recorded wavefield, the data,  $F$  is an integral operator, and  $\delta c$  is the perturbation in the density and/or elastic properties of the medium. In equation (1),  $u$  is corrected for the source and represents only the perturbed wavefield (e.g. underside reflections from the transition zone discontinuities), which is a function of the medium perturbation  $\delta c$ . These perturbations are measured relative to a given background model, e.g. ak135 or a regional tomographic model. The actual medium properties can be expressed as the combination of a background value (denoted by superscript 0) and a deviation from the background (superscript 1):

$$\rho(\mathbf{x}) = \rho^0(\mathbf{x}) + \rho^1(\mathbf{x}) \quad c_{ijkl}(\mathbf{x}) = c_{ijkl}^0(\mathbf{x}) + c_{ijkl}^1(\mathbf{x}) \quad (2)$$

where  $\rho$  is density,  $c_{ijkl}$  is the elasticity tensor, and  $\delta c = c_{ijkl}^1(\mathbf{x}) + \rho^1(\mathbf{x})$ .

The inverse problem estimates  $\delta c$  from the scattered wavefield  $u$ :

$$\delta c = (F * F)^{-1} F * u \quad (3)$$

The inversion takes as its input the preprocessed data  $u(\mathbf{x}^s, \mathbf{x}', y)$ , corrected for amplitude, phase, polarization, and travel time, including a source-term correction. Weights are applied according to geometry, and the expression is integrated over  $\mathbf{v}^m$ , i.e. over all isochrons. Bringing the source correction out of the term for  $u$  and writing  $\delta c$  as a

function of  $y$ ,  $\theta$ , and  $\psi$ , gives the expression for the GRT image point gather:

$$I(y, \theta, \psi) = \int_{E_{v,m}} \frac{u(y, \theta, \psi) \times |p^m|^3}{W(y, \theta, \psi) \times 2|w(y, \theta, \psi)|} dv^m \quad (4)$$

Here  $W$  is the source term correction, and  $w$  weights  $u$  according to the ray path: it accounts for changes in the stiffness tensor  $c_{ijkl}$  that describes the elastic parameters of the medium. Integration over  $\theta$  and  $\psi$

$$I(y) = \iint I(y, \theta, \psi) d\theta d\psi \quad (5)$$

yields the common image point gather at  $y$ . This last integration gathers all of the information into a single image of the medium perturbation.

#### 2.4 Application of the GRT to SdS data

The form of the GRT used in this study is somewhat simplified from the theory. We find that some of the subtleties of the GRT may be omitted with little effect, while others are beyond the scope of this study and are regarded as future work. For example, corrections for source, geometrical spreading, and ray path have not yet been applied. The weight we apply is a term to address the varying vertical resolution due to changes in scattering angle. Data corresponding to raypaths with large  $\theta$  are reduced by  $\cos(\theta/2)$  because of the  $\cos(\theta/2)$  error in the travel time predictions for a given scattering point.

We form image gathers for points in a vertical profile with a five-kilometer spacing, from zero to 1000 kilometers depth. Integration over  $\theta$  is carried out as the last step, because the vertical dilation with increasing  $\theta$  is useful information for characterizing the interface. The inversion result for each source-receiver pair is binned according to  $\theta$ . The size of the bins affects the final summed (integrated) image gather: large bins make the pulses in the final image gathers appear choppy and may lower the amplitude of the signal. The background velocity model from which the perturbations are measured smoothes the discontinuities over one hundred kilometers.

In summary, we implement the GRT by calculating the expected arrival time of scattered energy for a given path (i.e. source-receiver ( $s-r$ ) pair and image point), finding the amplitude of the data,  $u$ , at this arrival time, and repeating for all the  $s-r$  pairs. We apply weights according to  $\theta$ , integrate over  $\psi$  and  $\theta$ , and repeat for all image points along a vertical profile.

### 3. Data Selection and Preprocessing

The data used for this study are provided through IRIS, recorded at global networks through January 2005. We use  $SS$  waves and their precursors on the transverse component; the records are 2200 seconds long and begin 400 seconds before the predicted PP arrival. In order to avoid complications from the source, magnitudes are restricted to 5.5 – 6.8. Source depths are less than 50 km, in order to avoid the depth phase  $sSS$ , which bounces off the surface near the source before traveling downward. However, for shallow depths the depth phase is not simply absent; it arrives close in time to the  $SS$  phase and may complicate the signal. Tests are needed in order to determine if the GRT would erroneously map the depth phase to structure in the transition zone. If not, deep events may be more advantageous than shallow ones.

Epicentral distances from source to receiver range from  $90^\circ$  to  $170^\circ$ . For epicentral distances greater than  $170^\circ$ , non-specular ray paths may pass through the outer core, imposing an upper bound on epicentral distance, while the lower bound results from the polarity reversal of  $S_{660}S$  at  $90^\circ$ . The highest density of  $SS$  bounce points for data conforming to these parameters is in the Pacific ocean, due to the abundance of sources and receivers along the western part of the Pacific Rim and in North America (figure 3). We collected  $SS$  data with bounce points that fall within a  $20^\circ \times 20^\circ$  bin, centered at  $35^\circ$  latitude,  $170^\circ$  longitude. Figure 3B shows the density of midpoints in this region, grouped in  $0.5^\circ \times 0.5^\circ$  bins.

Owing to the large number of data that the GRT uses, the minimum signal-to-noise ratio can theoretically be quite low. Nonetheless, we visually examine the data, and eliminate data with a signal-to-noise ratio of less than 2, as given by the ratio between the  $SS$  amplitude and the noise level in the first few hundred seconds of the record, where no phases arrive. This improves the GRT results slightly. After weeding out data with low signal-to-noise ratios, we are left with slightly over 8000 data. Figure 3-B shows the

distribution of midpoints for data that meet all the abovementioned requirements.

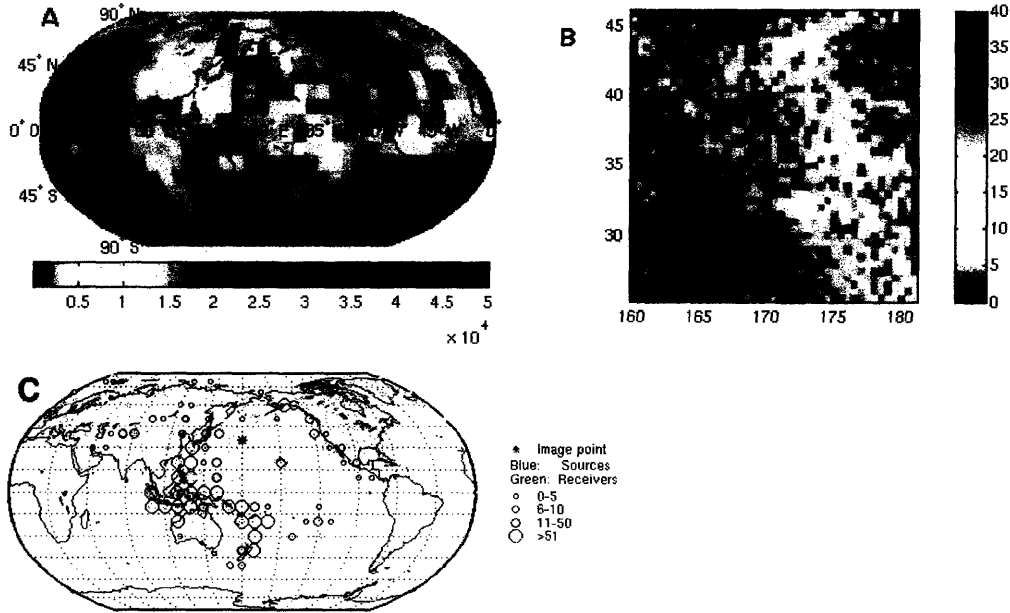


Figure 3. (A) Global distribution of *SS* bounce points for data with source-receiver distances of 80-180°, magnitude 5.5–6.8, and source depth 0-50 km. The blue rectangle outlines the 20°×20° area in which data are collected, shown in (B). (B) Distribution of *SS* bounce points of data used for the GRT, binned by half-degrees. (C) Distribution of sources and receivers. The pink square highlights the region in which data are collected. The size of the blue (green) circle indicates the number of sources (receivers).

The instrument response is deconvolved from the data, which are then bandpass filtered between 20 and 80 seconds. Filters with bandwidths of 10 – 50 and 15 – 50 seconds are also tested, in an attempt to utilize higher frequency data that could help to characterize the interface. These frequencies, however, produce GRT images with many oscillations of nearly constant amplitude that overwhelm the image gather, concealing everything but a weak signal from the ‘660’. The high frequency data may be used in future work to characterize the ‘660’ interface, but the data used for the results presented below are filtered between 20–80 seconds. Lastly, the *SS* signal is shifted to the predicted arrival time, and the entire record normalized with respect to the *SS* amplitude.

A record section of the transverse component, made using only the data within the 20°×20° bin studied here, shows the *SS*, *S<sub>410</sub>S*, and *S<sub>660</sub>S* arrivals (figure 4). The *SS* phase



is strongest because the stack was made by shifting the  $SS$  arrivals to the predicted  $SS$  travel time. The black dotted lines show the predicted arrival times of  $S_{410}S$  and  $S_{660}S$ ; faint stripes of red and blue can be seen beneath these lines, showing the arrival of energy of the  $SS$  precursors. Both phases are visible at distances less than  $130^\circ$ , though  $S_{660}S$  shows more strongly than  $S_{410}S$ . Data are most abundant for distances between  $90^\circ$  and  $140^\circ$ , giving the edges of the plot a grainy appearance. Unexpectedly, the  $PS$  and  $PPS$  phases appear in the plot. Since no  $P$ - $SH$  conversion is expected for horizontal interfaces, this may indicate topography on the interface from which they reflect, or anisotropy along the raypath, or problems with the orientation of the sensors. The effect of the presence of these phases on the GRT will be explored before publication of the results.

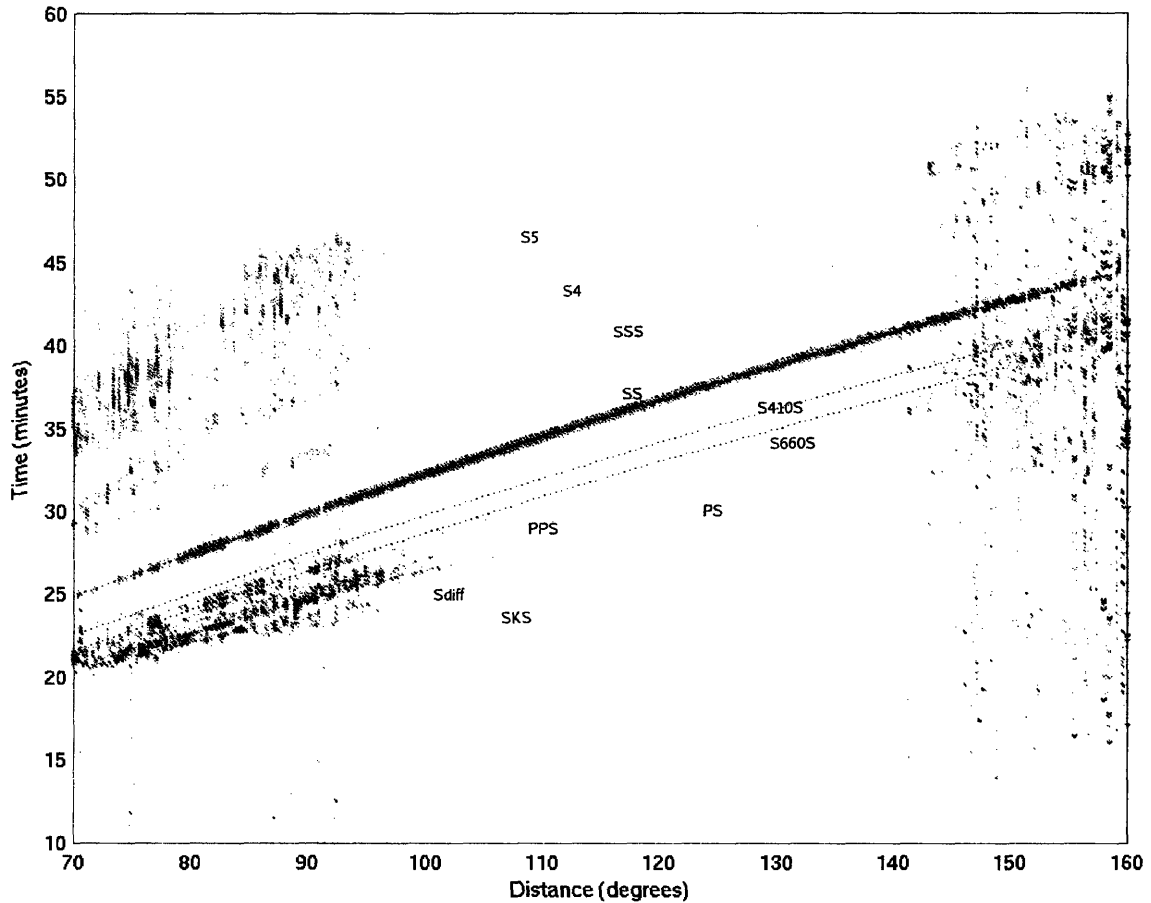


Figure 4. Stack of data from the study area. The stack is relative to the  $SS$  phase. The predicted arrival time of the  $SS$  precursors is shown by the dotted black lines.

#### 4. Synthetic tests

Before applying the GRT to the observed data, we first test it on synthetic waveforms. Our goal in doing so is to ensure that the GRT maps the discontinuities to the appropriate depths and that the results display the expected dilation with increasing scattering angle. Synthetic testing also allows us to investigate the expected amplitudes of the signals, the vertical resolution, the extent of sidelobes and whether they resemble structure at depth, and the effect of multiple reflections.

Synthetics of  $SS$ ,  $S_{410}S$ , and  $S_{660}S$  data are made using the WKB method, with the same source function for all waveforms, and filtered using a bandwidth of 20–80 seconds. We first use synthetics to which we have applied a Hilbert transform (figure 5), which gives a representation of the total energy of the arrival. However, the GRT images produced from the observed data are found to be clearest with data that have not undergone the Hilbert transform. In order to compare the observed and synthetic data results, we also test synthetics without the Hilbert transform (figure 6). The GRT using the Hilbert-transformed synthetics is included here in order to demonstrate the dilation of the signal, showing only the signal at 660 km depth, since the dilation is most visible in this case. However, we direct most of the attention to the features of the GRT that uses non-Hilbert-transformed synthetics.

The GRT, integrated over scattering angle and azimuth, yields a vertical profile of oscillations that represent variations of elastic parameters and/or density from the background model; plotting the GRT before integration over scattering angle,  $\theta$ , demonstrates the dilation of the signal with increasing  $\theta$ . Synthetic results show signals that peak at depths of 0, 410, and 660 km (figures 5 and 6). The peaks at 410 and 660 km are comparable in amplitude. The expected dilation is clearly present in both GRT tests, with the width of the peak increasing by a factor of  $1/\cos(\theta/2)$ .

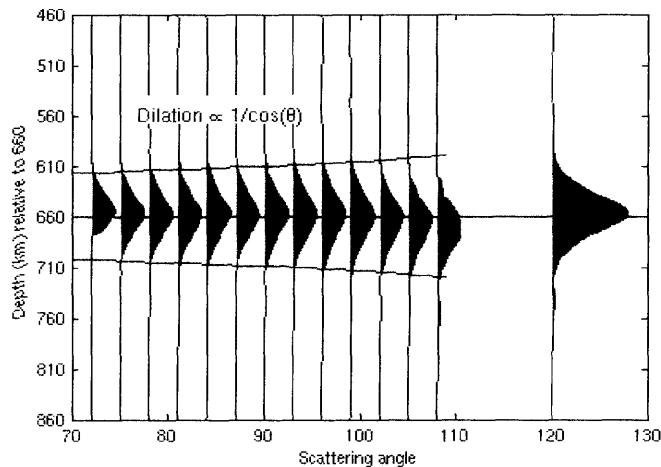


Figure 5. GRT results using synthetic data to which a Hilbert transform has been applied, showing only the signal from the '660'. Dilation of the signal is noticeable but subtle. This is because the range of scattering angles for the geometry of *SS* and its precursors is small, and excludes angles for which the dilation is most obvious.

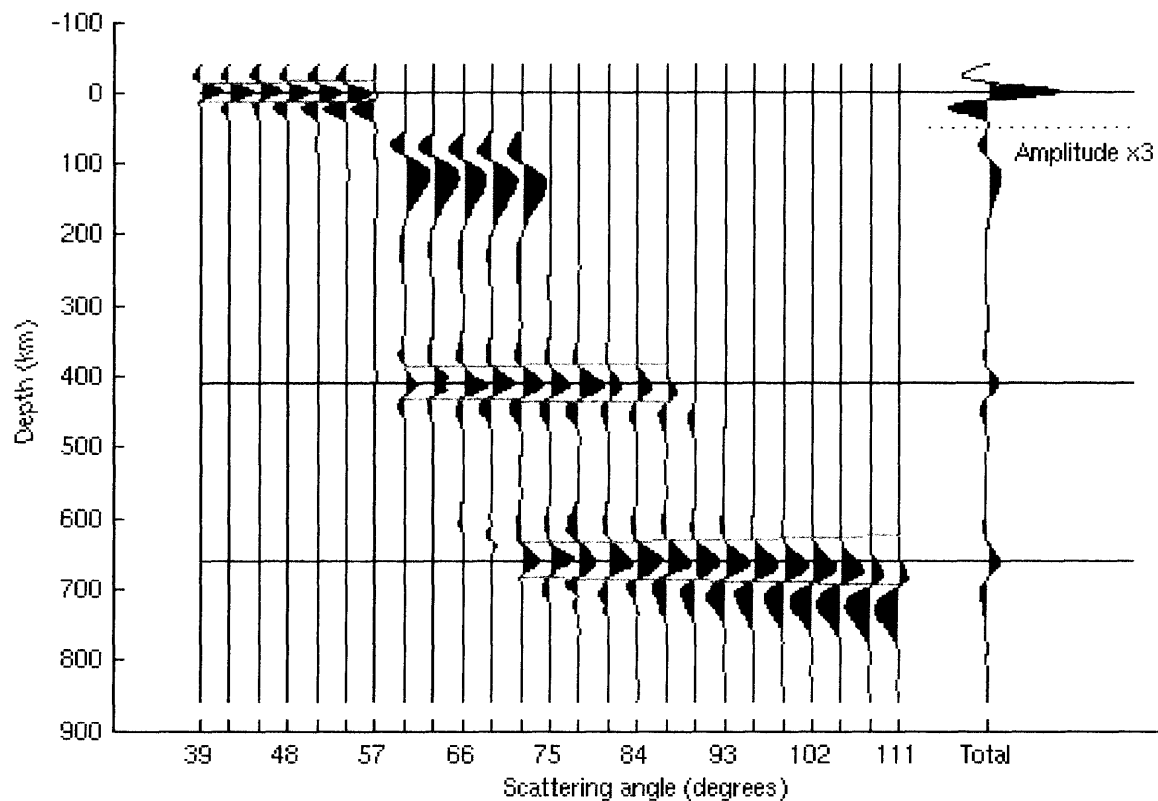


Figure 6. Synthetic test of the GRT using data that have not been through the Hilbert transform. Sidelobes of the 410 and 660 signals are comparable in width to the main peaks but are much smaller in amplitude, and have the opposite polarity. Sidelobes of the surface signal are more extensive and similar in amplitude to the 410 and 660 signals. Dilation of the signal with increasing  $\theta$  (scattering angle), marked by the green lines, is present but subtle. The amplitude of the common image gather below the dotted line is increased in order to show the signal at depth more clearly.

The peak in figure 5, which is made with synthetics that undergo the Hilbert transform, is about 100 km wide at its base. Figure 6, which is more relevant to the results we obtain with the observed data, shows widths of the 410 and 660 peaks, excluding the sidelobes, of about 50 km. The widths of the peaks for both sets of synthetic data are independent of the depth range over which the discontinuities are smoothed.

Sidelobes are present in the GRT results for the non-Hilbert-transformed data (figure 6). The 410 and 660 signals have sidelobes that extend 40 to 50 km in each direction and are 1/3 to 1/2 the amplitude of the main peak. There are no secondary sidelobes. The surface signal, because of its greater amplitude, has multiple sidelobes, including a positive lobe that peaks at about 125 kilometers depth. This lobe has the same, or greater, amplitude as the 410 and 660 signals; care should be taken not to confuse this sidelobe with a reflector at depth.

The GRT is not designed to use multiply scattered waves, and it is possible that multiple reflections would map to non-existent structure. Therefore, we examine the effect on the GRT of multiples from the surface or the transition zone discontinuities. Adding a multiple phase to the synthetics of the  $SS$ ,  $S_{410}S$ , and  $S_{660}S$  synthetics that reflects once between the '410' and '660' discontinuities does not affect the GRT image gather. Other multiples from the surface, '410', or '660' would not show in the GRT image, as these reflect from the surface, arrive later than the  $SS$  phase, and would therefore map to a scattering point above the surface. Other phases that may affect the GRT images include  $PS$ ,  $PPS$ , and depth phases such as  $sS$ .  $PS$  and  $PPS$  arrivals, which show strongly in the record section of figure 4, may be erroneously mapped to structure deeper than 660 km, while depth phases could interfere with shallower structure; these effects will be investigated in future work.

The synthetic tests provide a reference against which we can compare the GRT results that use recorded data. We may expect to see signals at or near 410 and 660 kilometers depth that are about 50 km wide, comparable in amplitude, and have small sidelobes that are unlikely to be mistaken for additional reflectors. Signals that peak at depths less than ~150 km depth should be interpreted conservatively, since sidelobes of the surface signal extend to this depth.

## 5. Results

Application of the GRT to our data produces results that show strong structure at depths near 410 and 660 kilometers. The GRT also images structure at several other depths, including 520 km. In this section we discuss the main features of the GRT results: the plots of scattering angle vs. depth, the topography on the ‘410’, ‘520’, and ‘660’ and the thickness of the transition zone, the relative amplitudes of the observed signals, and other structure whose origins are uncertain.

Excluding data whose *SS* bounce points are farther than  $3^\circ$  from the image point gives the most stable results, while the amount of data in each bin affects the image gather very little (figure 7). The width of the peaks is about 50 – 90 km, large compared to the width of the synthetic peaks. This may be because the synthetics were made using a step discontinuity while the actual transition zone discontinuities occur over a depth range. The ‘660’ peak in particular has a greater width than the synthetic ‘660’; this may also be due to interference with adjacent peaks.

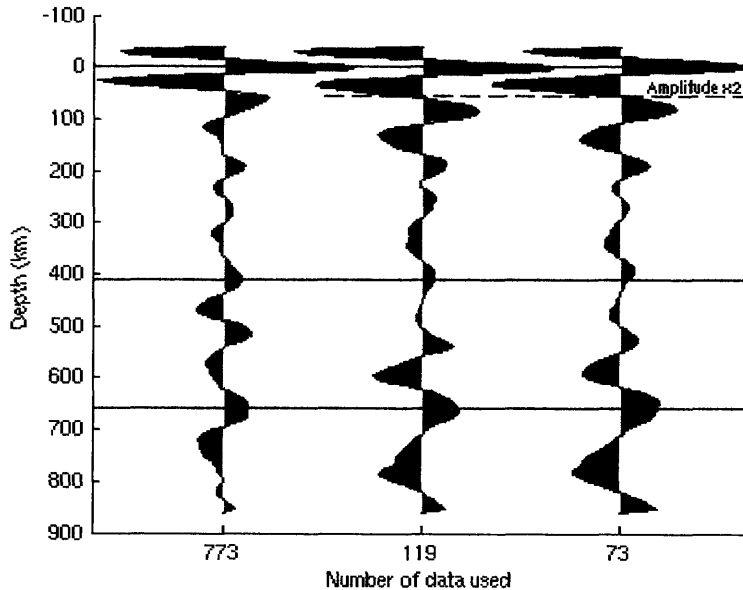


Figure 7. Dependence of the GRT on the number of data used. In the middle and right traces, the amplitude above the dotted line is increased by a factor of two relative to the rest of the trace. The only significant change incurred by using fewer data is a decrease in the strength of the surface signal relative to the rest of the profile.

The image gathers before integration over  $\theta$  are too messy to be useful (figure 8). The image gather for each scattering angle is quite different in appearance from the final image gather. This may be due to the variability in data quality, and the large range of velocities from the top to the bottom of the vertical profile. Because velocity varies hugely with depth, mapping data to different depths also maps them to different scattering

angles. So long as the data quality is consistent, this does not matter. If, however, the data at certain epicentral distances are significantly better than others, or of a much larger amplitude, peaks corresponding to these data may show at different depths for each scattering angle and, because of their large amplitude, overwhelm the image gathers for each scattering angle. When summed, however, they produce an intelligible profile that incorporates the contributions from all the data. This is what is seen with our data. The scattering angle plots are unusable, but the common image gather is clear and reliable.

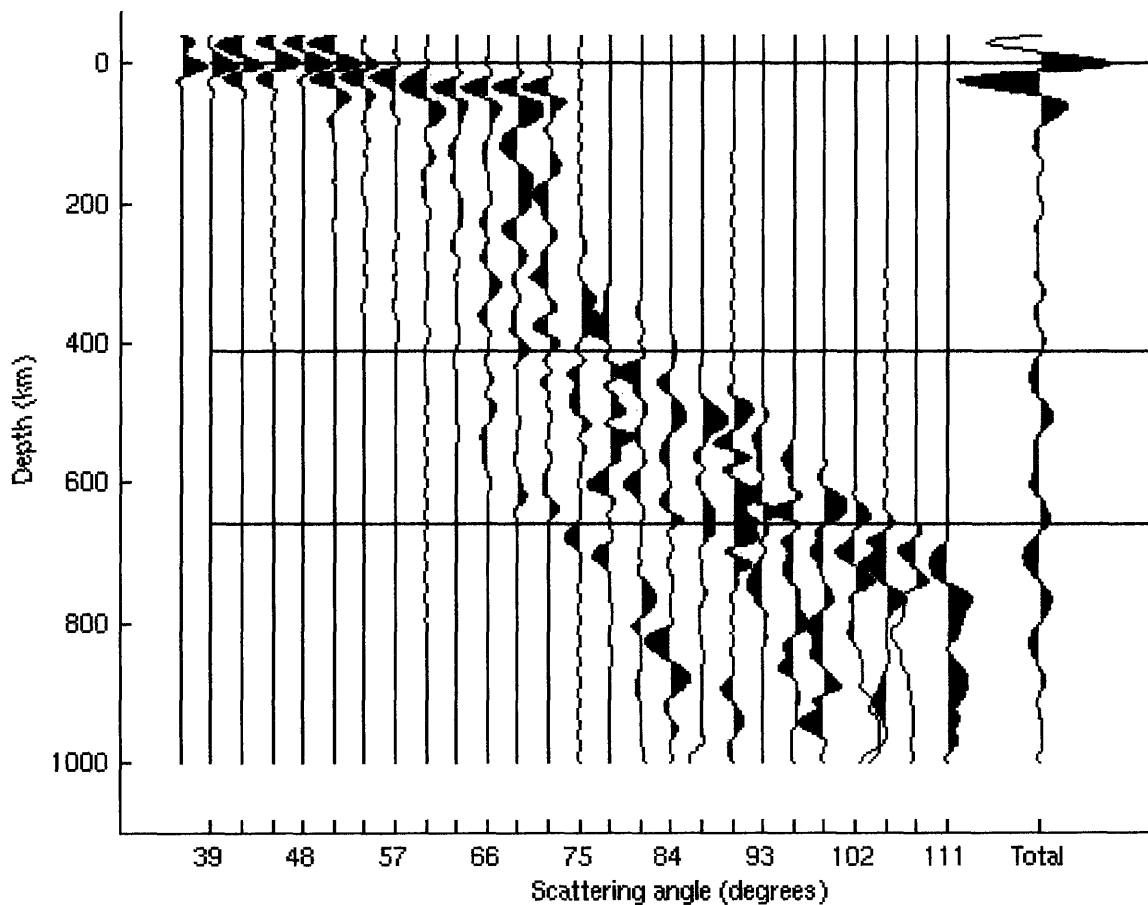


Figure 8. GRT image gathers at 35° latitude and 175° longitude before and after integration over scattering angle. Only after the final integration does the image gather yield intelligible results. The surface signal is clean because the SS phase is shifted to the predicted SS arrival time before running the GRT. Peaks at 410, 520, and 660 appear, as well as shallower and deeper signals. Without comparing it to adjacent profiles, it is difficult to distinguish what is meaningful signal.

Creating several adjacent common image gathers allows one to see the consistency and the variations of the structure, as well as to distinguish between signal and noise. We present three fine-scale cross-sections of the mantle, shown in figure 10, which extend from the surface to 1000 kilometers depth. The locations of these cross-sections are shown in figure 9. Tables A, B, and C list the depths of the ‘410’, ‘520’, and ‘660’ at each location shown in the cross-sections of figure 10.

In figure 10A, of the expected signals arising from the transition zone discontinuities, the ‘660’ is the strongest, followed by the ‘520’; the ‘410’ is the weakest of the three. This is a surprising result, since previous studies have found that the ‘520’ is generally the weakest (e.g. *Flanagan and Shearer, 1998a; Gu and Dziewonski, 2002; Chambers et al., 2005a; Deuss et al., 2006*). In addition to these three, the cross-section shows strong, laterally continuous peaks at about 175, 300, 800, 950, and 870 – 900 km, though none of these extend throughout the entire cross-section, suggesting that they are laterally intermittent features. A marked change occurs at 175° longitude. Image gathers both to the east and west of this point show continuous, but different, structure. At 176°, the ‘660’ seems to split into two peaks: a main one and a small side peak. With increasing distance eastward, this secondary peak becomes deeper, while the main peak moves shallower. Westward of 176°, only one strong peak is observed around 660 km depth. Concurrent with, and perhaps because of, the appearance of the secondary peak, the strong signal around 800 km depth shifts downward, and a peak around 950 km depth appears while the peak at 880 km disappears. In addition, the ‘410’ and ‘520’ deflect upward by 15–25 kilometers over several degrees, and new, strong peaks around 300 and 175 km appear.

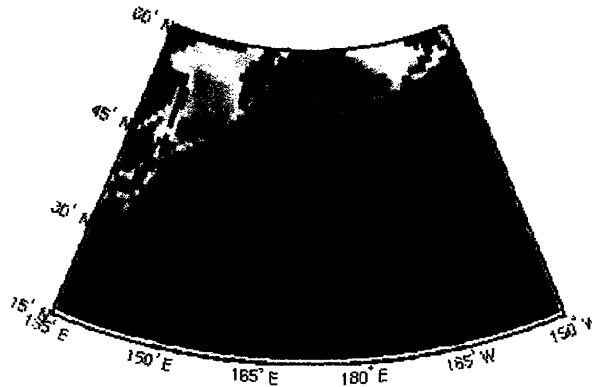


Figure 9. Locations of the cross-sections in figure 10.

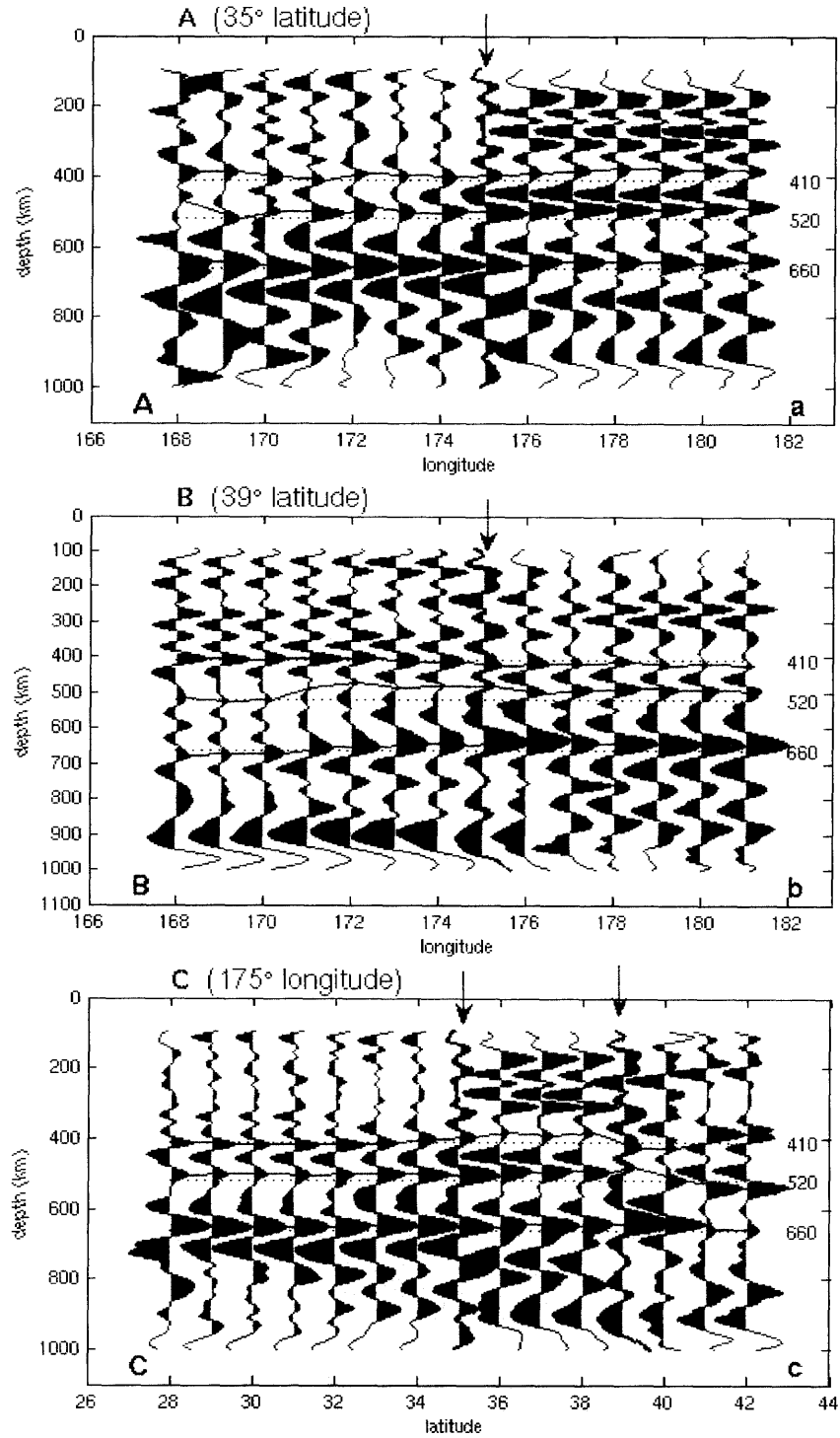


Figure 10. Cross-sections made by plotting adjacent vertical profiles; locations shown in figure 9. The surface signal is excluded to highlight the weaker structure. Each trace is normalized by its maximum. The '660', '520', and '410' are continuous throughout all three sections; the '660' dominates the figures. Arrows and bold lines highlight locations where the cross-sections intersect; profiles pointed to by the same color of arrow are one and the same.



At 655 kilometers, the '660' is deepest at 170° longitude, and shallows progressively eastward until, at 181°, it peaks at 640 km. The '520' and '410' also become shallower from west to east, with comparable magnitudes of variation. Comparing this cross-section to a cross-section made with synthetic data (figure 11), using the same geometry of sources and receivers, shows that the depths are not affected by the geometry, or are affected very little.

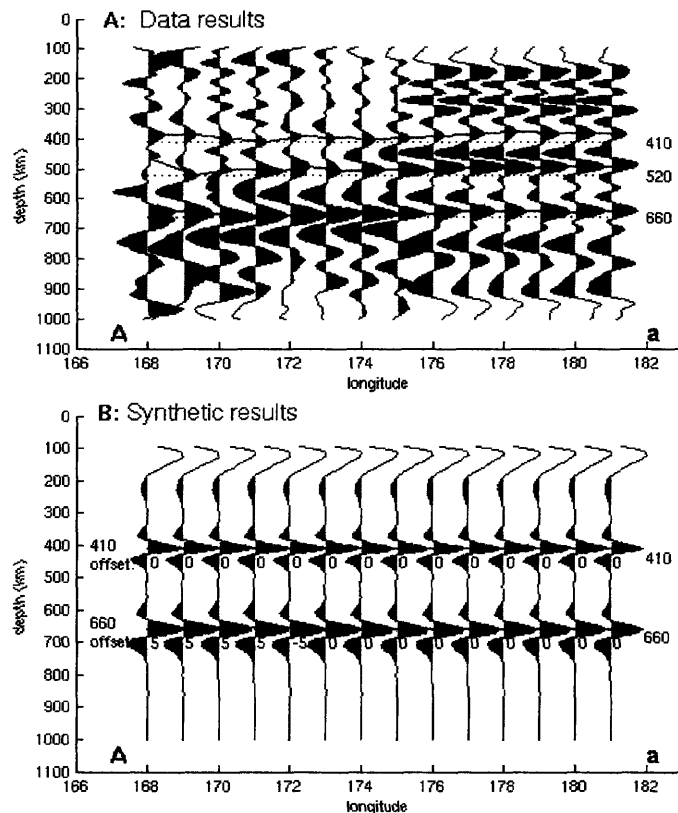


Figure 11. Comparison between data (A) and synthetic (B) results from the GRT, for the same source-receiver geometry. The location is the same as that of figure 10-A, shown in figure 9 by the A-a line. The synthetic results show that variation in the geometry of each profile causes very little vertical offset, if any.

The cross-section shown in figure 10-C intersects the cross-section of figure 10-A at (35, 175). This figure shares some of the same features as those of figure 10-A. The relative amplitudes of the '660', '520' and '410' are similar, with the '660' being the strongest and the '410' the weakest, except for latitudes 28–32 where the '520' is of approximately the same amplitude as the '410'. The '660' seems to split into two peaks for part of the cross-section (latitudes 36–38, possibly 39 and 40), though it is less clear

than in 10-A. The topography, however, is quite different. The depth of the '660' remains at 640–645 km depth, which, given the 5 km spacing between image points along the vertical profiles, can be considered constant. The '520' is also nearly constant; it stays at 500 km depth from 28°–35° latitude, and then deepens to 540 km for the more northern latitudes. The '410' depth jumps around more than the '520' and the '660', but the general trend is a shallowing from south to north by about 35 kilometers, with huge jumps in depth over the northern few degrees.

The cross-section of figure 10-B samples structure along the 39-degree latitude line, from 168°–181°. The '660' is still the strongest and most consistent signal, and the '410' is weaker but continuous. The '520', however, is absent or extremely weak throughout the western part of the cross-section; at 175° it appears and is westward continuous, where its amplitude is comparable to the '410'. The '660' here shows a similar trend as in the parallel cross-section 4° to the south; it is deepest in the west, at 670 km, and shallows to 635 km in the east. The '520' is absent for the western half of the profile, appearing at an average depth of 490 km from 176° to 181°. The '410' lies at 410 km in the west, deepening to 420 km in the east. Signals in the upper mantle and around 750 and 1000 km are also observed, though the upper mantle signals are messy and it is difficult to discern if they represent real structure. The topographies of the '410' and '660' appear to be anti-correlated; this is not the case in figure 10-A, where the depths seem to display a positive correlation, nor in figure 10-C, where there seems to be no correlation, positive or negative (see figure 12).

The transition zone thicknesses in figure 10 vary by  $\pm 10$ –30 km from the average thickness (257, 238, and 243 km in figures 10–A, B, and C, respectively). Figure 12 shows that the thickness is strongly anti-correlated with the depth of the '410' reflector, while there is little correlation with the depth of the '660'. The depths of the '410' and '660' do not seem to be correlated; however, looking at the correlations within each individual cross-section leads one to believe that, rather than no correlation, there may be both a positive and a negative correlation.

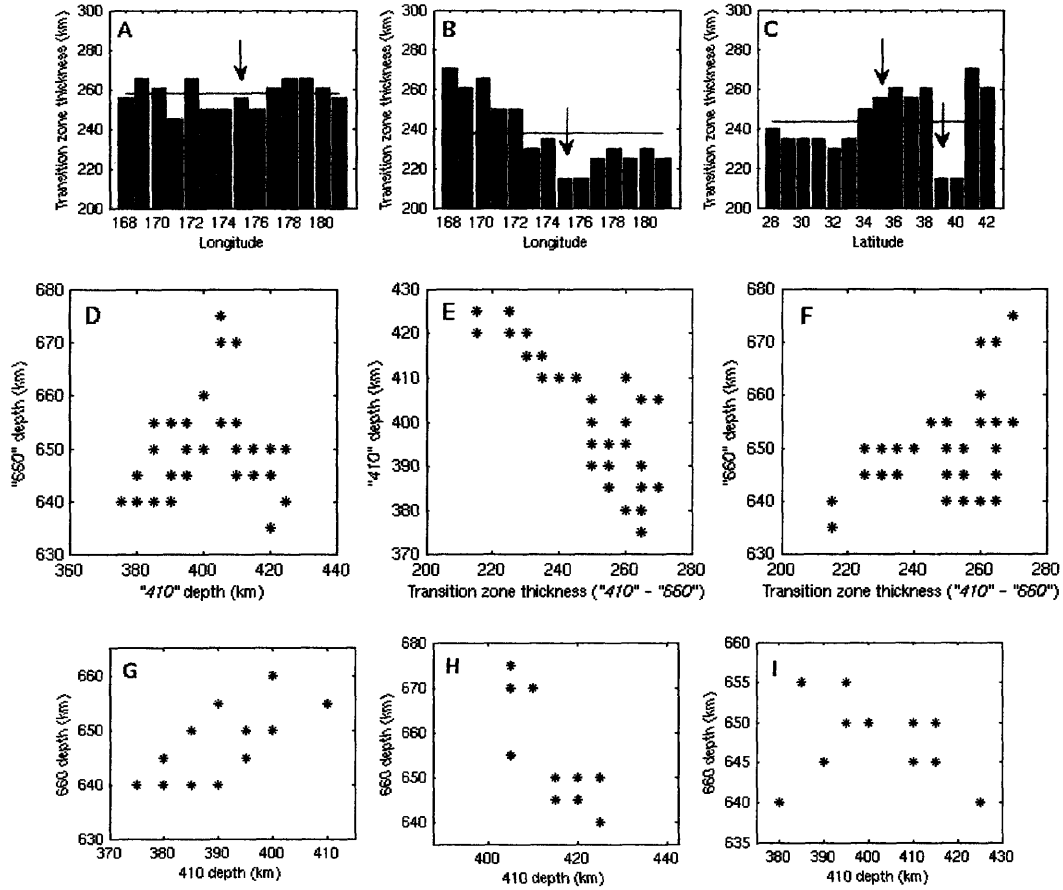


Figure 12. **A-C**: Thickness of the transition zone (the difference between '660' and '410') along the profiles of figures 10-A, B, and C, respectively. Red lines show the average thickness of each cross-section. **A** shows almost no variation from its average depth of 257 km, though the depths of the reflectors themselves vary considerably (figure 10; tables A, B, C); **B** shows thinning with increasing distance eastward, with an average depth of 238 km; **C** shows thickening with increasing distance northward, with an average depth of 243 km. As in figure 10, the arrows show locations where the cross-sections intersect. **(D)** Correlation between the depth of the '410' and '660' for all locations. The correlation is weak or absent, but could be a combination of a positive correlation for shallow '410' depths, and a negative correlation for deeper '410' depths. This plot is broken down for each cross-section in plots G through I. **(E)** The depth of the '410' is strongly anti-correlated with the thickness of the transition zone. **(F)** The depth of the '660' appears to be weakly positively correlated with transition zone thickness. **(G)** The '410' and '660' depths for the cross-section of figure 10-A, at 35 latitude, showing a positive correlation. **(H)** The depths of the '410' and '660' of figure 10-B show a negative correlation. **(I)** Correlation of the depths in figure 10-C; no correlation is present, though if the two data points in the lower left corner are regarded as outliers, the plot shows a strong negative correlation.

## 6. Discussion

The GRT successfully images the '410', '510', and '660' discontinuities in cross-sections that extend to 1000 kilometers depth. The success of the GRT in imaging mantle structure and the diversity within the cross-sections is striking. The depth of the signals, as well as their shape and amplitude, varies widely over only 13° of longitude (or, for the longitudinal profile, 15° of latitude). At 35° latitude, at a depth of 660 km, this translates to 1,061 km; at 39°, 1,007 km.

As previously mentioned, reflections from the '520' are generally weaker than reflections from the '410' and '660', and are often not observed at all (*Flanagan and Shearer, 1998a; Helffrich, 2000; Gu and Dziewonski, 2002; Chambers et al., 2005a; Deuss et al., 2006*). This may seem to contradict the results presented here of a strong, continuous '520'. In two of the cross-sections, it is a pervasive feature over the entire image; the third cross-section shows the '520' strong and continuous in the eastern part, and absent in the west. In the north/northwest Pacific, however, reflections from the '520' do appear in waveform data. *Flanagan and Shearer (1998a)* and *Gu et al. (2003)* find that, in this area, the '520' is shallow by about 10 km, and the amplitude of the '520' signal is comparable to those of the '410' and '660'. There is thus little or no discrepancy for this region of the Pacific. The difference in the strength of the '520' signal reported here and elsewhere may arise from the resolution of the respective studies. Previous studies average the reflections from the '520' over a very large area; perhaps if the GRT profiles for every point in the 20°×20° bin were arbitrarily summed, averaging over areas where the '520' is strong and areas where it is absent would result in an image where the '520' is weaker than both the '410' and '660'. This was done for the profiles in the cross-section, but since the '520' is a strong feature within each of the sections, the summed image also showed a strong '520'. In order to see if summing the image gathers results in similar profiles as seen in other studies, we would need to sum over the entire geographic region.

The '520' is generally elusive, but whether this is because it sometimes does not produce reflections at all or because the reflections are of such small amplitude that they can not be detected in noisy data is controversial. Our results suggest that the former is more applicable, since the GRT images structure even with noisy data, and yet we observe huge variations in the strength of the '520' in the image gathers of figure 10. If

the '520' arises from the  $\beta$ - $\gamma$  phase change, it is unlikely to be a globally detectable discontinuity. Waves would be only weakly reflected by the small velocity contrast created by these two phases, and the wide region of coexistence would make the transformation invisible to all but low frequency waves (*Fei and Bertka, 1999*). The large Clapeyron slope, as well as the strong dependence of transition pressure on the concentration of iron, could cause the depth at which the phase change occurs to vary widely on scales that are small relative to the size of the area usually averaged by studies of the transition zone. Phase changes around 520 km also occur in the  $\text{MgSiO}_3$  system, which could contribute to the '520' signal. The fact that we detect such a strong signal from the '520' suggests that the change in the pyroxene system may be at least partly responsible for the signal.

The sharp change in features that occurs near the center of figures 10-A and 10-C may be an artifact. It does not seem to coincide with areas of more or fewer data. It is possible that it results from complications from the source mechanism. Since each profile utilizes the scattered energy from data whose specular reflections lie within  $3^\circ$  of the image point, one anomalous record could affect 7 adjacent depth profiles, though each profile would sample a different part of the waveform. This "sharing" of the records between image points does not mean the energy is smeared over  $6^\circ$ ; it results from the consideration of both specular and non-specular energy arrivals. Deconvolving the data from the source function and extending the cross-sections over greater distances should help to determine what is a continuous signal and what is intermittent.

The large amplitude signals that occur below 660 km may be caused by incorrect mapping of *PS* or *PPS* phases. The effect of these phases on the GRT will be investigated in future work, by running the GRT on synthetics of *PS* and *PPS*. If, however, these features are real, they are unlikely to be continuous over long distances. If they were global features, surely they would have been observed before. It is possible that the current standard view of the mantle as largely featureless is greatly oversimplified, and that chemical heterogeneities are more common than we think. Phase changes outside of the olivine system also may affect the image, as they are likely to cause reflections with large fluctuations in strength and depth (*Fei and Bertka, 1999*).

The depths of the '410', '520', and '660' generally agree with observations from other studies (*Flanagan and Shearer, 1998a; Rost and Weber, 2002; Gu et al., 2003;*

*Chambers et al.*, 2005a; *Chambers et al.*, 2005b), which resolve structure on the order of 1000 km. All three are shallower than or at the same depth as the averages for which they are named. Our results also show shallow depths for the '410', '520', and '660' discontinuities. Transition zone thicknesses vary from 215 to 270 kilometers, with an average thickness of 246 kilometers. This average and the magnitude of the variations from the average agree nicely with the global average of ~250 kilometers and deviations of  $\pm 10$ -25 kilometers found in the literature (*Bock et al.*, 1995; *Chevrot et al.*, 1999; *Gu et al.*, 1998; *Gu and Dziewonski*, 2002; *Lebedev et al.*, 2002a; *Li et al.*, 2002).

The correlation plots shown in figure 12 show that topography on the '410' controls transition zone thickness. This precludes the possibility that the topography on the three transition zone discontinuities can be explained by a temperature anomaly that extends through the entire transition zone, over the entire region encompassing all three cross-sections. We must therefore turn to the many other factors that affect topography in order to explain our observations. Shallow '410' depths could imply a colder mantle, or a higher concentration of iron, water, aluminum, or other trace elements, or any combination of these (*Wood*, 1995; *Irfune and Isshiki*, 1998). A shallow '660' can result from a hotter mantle; the depth is, to first order, independent of iron and water content, though aluminum may influence the depth (*Wood and Rubie*, 1996; *Fei and Bertka*, 1999; *Higo et al.*, 2001).

Assuming for now that the topography on the '410' is caused solely by temperature anomalies, we can estimate the temperature of the mantle from the '410' depths at each image point. Given the Clapeyron slope of the  $\alpha$ - $\beta$  phase change of 3 MPa/K, and using the approximation 1 GPa  $\cong$  30 km, the variations of up to  $\pm 25$  km from the median '410' depth translate to temperature anomalies of  $\pm 280$  K. This must be an upper bound to the thermal variations, since varying composition can also affect topography. However, it is premature to infer either temperature or composition from the topography seen in the cross-sections of this study. The absolute depths may be affected by the source mechanism, and it is unclear how variations in the background velocity model affect the discontinuity depths.

Despite the uncertainties, the results are promising. We are able to map structure on a finer scale than previously possible. We observe topographies that vary widely over only a few hundreds of kilometers. Though the error in the absolute depths of the

discontinuities due to variations in the background velocity model is undetermined, the topography is robust, since any error in the model is applied equally to all image points, provided they sample similar enough ray paths. We are able to show a correlation between topography on the '410' and transition zone thickness. Finally, though the analysis may be premature, we give an upper bound to the thermal variations that may cause the observed topography on the '410' of  $\pm 280$  K.

## 7. Conclusion

Application of the GRT to the transition zone discontinuities produces images unprecedented in their resolution and clarity. Imaging deep mantle structure on such a small scale not only gives detailed information about the topography of the discontinuities, it also provides redundancy that lends credence to the depth determinations. Where previous studies find one depth for an area on the order of 1000 kilometers, the GRT yields depths every  $1^\circ$ —about 111 kilometers. Results show very clear signals for the '410', '520', and '660' phases, as well as several interesting and surprising features that require further investigation. Topographies vary by 50, 70, and 40 km, peak-to-peak, on the '410', '520', and '660', respectively; average depths are shallower than the global averages for all three reflectors, at 400, 500, and 650 kilometers depth. The thickness of the transition zone averages 245 km, with variations of  $\pm 25$  km, which correlate strongly with the depth of the '410'. The correlation between the depths of the '410' and '660' is different in each cross-section; in 10-A, the depths display a slight positive correlation; in 10-B, a negative correlation; and in 10-C, no correlation. The interpretation of these features must include variations of both temperature and composition on small enough scales to account for these features.

Work to be completed in the immediate future includes deconvolving the source from the data and increasing the bin size within which data are collected in order to make longer profiles. This will illuminate the nature of the structure outside of the transition zone and determine whether it is continuous over large distances or not. Synthetics of *PPS* and *PS* phases will be created and used to test the effect these phases have on the GRT, to see if they can account for the strong signals at depth. We will also test the effects of phases from deep events, such as *sS*, and if they do not adversely affect the GRT, we will extend the data set to include deep events. Long term goals involve

characterizing the discontinuities and ascertaining the relationship between GRT results and mantle chemistry and temperature. Even at this early stage, the GRT has shown to be an extremely powerful tool for imaging the deep earth, but the capacity of the GRT to provide high-quality, high-resolution information on earth's structure and thermal and chemical makeup has yet to be fully realized.



## Tables

A: 35° latitude line														
<i>longitude</i>	168	169	170	171	172	173	174	175	176	177	178	179	180	181
'410'	385	385	400	410	390	395	400	395	390	380	375	380	380	385
'520'	470	520	500	505	490	505	500	505	495	495	495	490	490	485
'660'	640	650	660	655	655	645	650	650	640	640	640	645	640	640
<i>Thickness</i>	255	265	260	245	265	250	250	255	250	260	265	265	260	255

B: 39° latitude line														
<i>longitude</i>	168	169	170	171	172	173	174	175	176	177	178	179	180	181
'410'	405	410	405	405	405	415	415	425	420	420	415	425	420	425
'520'	515	525	520	485	470	485	480	480	500	490	485	490	490	495
'660'	675	670	670	655	655	645	650	640	635	645	645	650	650	650
<i>Thickness</i>	270	260	265	250	250	230	235	215	215	225	230	225	230	225

C: 175° longitude line															
<i>latitude</i>	28	29	30	31	32	33	34	35	36	37	38	39	40	41	42
'410'	410	415	415	415	415	410	400	395	380	390	380	425	425	385	395
'520'	505	500	500	505	500	500	505	505	495	490	495	480	520	540	540
'660'	650	650	650	650	645	645	650	650	640	645	640	640	640	655	655
<i>Thickness</i>	240	235	235	235	230	235	250	255	260	255	260	215	215	270	260

Tables A, B, and C: Depth of the transition zone discontinuities and the thickness of the transition zone (the difference between the depths of the '660' and '410') in kilometers. Values are shown for each location in the cross-sections of figure 10.

## References

- Benz, H.M. and Vidale, J.E., 1993. Sharpness of upper-mantle discontinuities determined from high-frequency reflections. *Nature* 365, pp. 147–150
- Bercovici, D., and Karato, S., 2003. Whole-mantle convection and the transition-zone water filter. *Nature* 425, pp. 39–44
- Beylkin, G., 1985. Imaging of discontinuities in the inverse scattering problem by inversion of a causal generalized Radon transform. *J. Math. Phys.* 26, pp. 99–108.
- Bina, C.R. and Helffrich, G.R., 1994. Phase transition Clapeyron slopes and transition zone seismic discontinuity topography. *J. Geophys. Res.* 99, pp. 15853–15860.
- Bock, G., et al., 1995. On the discontinuities in the upper mantle. *Phys. Earth Planet. Inter.* 92, pp. 39–43.
- Castillo, J., et al., 2001. Wavelet transform: A tool for the interpretation of upper mantle converted phases at high frequency. *Geophys. Res. Lett.* 28, pp. 4327–4430.
- Castle, J.C. and Creager, K.C., 2000. Local sharpness and shear wave speed jump across the 660-km discontinuity. *J. Geophys. Res.* 105, pp. 6191–6200.
- Chaljub, E. and Tarantola, A., 1997. Sensitivity of *SS* precursors to topography on the upper mantle 660-km discontinuity. *Geophys. Res. Lett.* 24, pp. 2613–2616.
- Chambers, K., et al., 2005a. Reflectivity of the 410-km discontinuity from *PP* and *SS* precursors. *J. Geophys. Res.* 110(B02301), doi:10.1029/2004JB003345.
- Chambers, K., et al., 2005b. Topography of the 410-km discontinuity from *PP* and *SS* precursors. *Earth Planet. Sci. Lett.* 235, pp. 610–622.
- Chevrot, S., et al., 1999. Global scale analysis of the mantle *Pds* phases. *J. Geophys. Res.* 104, pp. 20203–20219.
- Deuss, A., and Woodhouse, J., 2001. Seismic observations of splitting of the mid-transition zone discontinuity in earth's mantle. *Science* 294, pp. 354–357.
- Deuss, A., et al., 2006. The nature of the 660-kilometer discontinuity in Earth's mantle from global seismic observations of *PP* precursors. *Science* 311, pp. 198–201.
- Fei, Y., et al., 1999. Phase transitions in the Earth's mantle and mantle mineralogy. *Mantle Petrology: Field Observations and High Pressure Experimentation: A Tribute to Francis R. (Joe) Boyd*, The Geochemical Society, Special Publication No. 6, pp. 189–204.
- Fei, Y., et al., 2004. Experimentally determined postspinel transformation boundary in  $\text{Mg}_2\text{SiO}_4$  using  $\text{MgO}$  as an internal pressure standard and its geophysical implications. *J. Geophys. Res.* 103(B02305), doi:10.1029/2003JB002562.
- Flanagan, M.P. and Shearer, P.M., 1998a. Global mapping of topography on transition zone velocity discontinuities by stacking *SS* precursors. *J. Geophys. Res.* 103, pp. 2673–2692.

- Flanagan, M.P. and Shearer, P.M., 1998b. Topography on the 410-km seismic velocity discontinuity near subduction zones from stacking of *sS*, *sP*, and *pP* precursors. *J. Geophys. Res.* 103, pp. 21,165–21,182.
- Gaherty, J.B., et al., 1999. Testing plausible upper-mantle compositions using fine-scale models of the 410-km discontinuity. *Geophys. Res. Lett.* 26, pp. 1641–1644.
- Gu, Y., et al., 1998. Global de-correlation of the topography of transition zone discontinuities. *Earth Planet. Sci. Lett.* 157, pp. 57–67.
- Gu, Y.J., and Dziewonski, A.M., 2002. Global variability of transition zone thickness. *J. Geophys. Res.* 107(B7), doi:10.1029/2001JB000489.
- Gu, Y.J., et al., 2003. Simultaneous inversion for mantle shear velocity and topography of transition zone discontinuities. *Geophys. J. Int.* 154, pp. 559–583.
- Helffrich, G., and Bina, C.R., 1994. Frequency dependence of the visibility and depths of mantle seismic discontinuities. *Geophys. Res. Lett.* 21, pp. 2613–2616.
- Helffrich, G., 2000. Topography of the transition zone seismic discontinuities. *Reviews of Geophys.* 38, pp. 141–158.
- Higo, Y., et al., 2001. Effect of water on the spinel-postspinel transformation in  $\text{Mg}_2\text{SiO}_4$ . *Geophys. Res. Lett.*, 28, pp 3505–3508.
- Hirose, K., et al., 2001. In situ measurements of the phase transition boundary in  $\text{Mg}_3\text{Al}_2\text{Si}_3\text{O}_{12}$ : implications for the nature of the seismic discontinuities in the Earth's mantle. *Earth Planet. Sci Lett.* 184, 567–573.
- Hirose, K., 2002. Phase transitions in pyrolitic mantle around 670-km depth: Implications for upwelling of plumes from the lower mantle. *J. Geophys. Res.* 107(B4), 10.1029/2001JB000597.
- Irifune, T., et al., 1998. The postspinel phase boundary in  $\text{Mg}_2\text{SiO}_4$  determined by in situ X-ray diffraction. *Science*, 279, pp. 1698–1700.
- Irifune, T. and Isshiki, M., 1998. Iron partitioning in a pyrolite mantle and the nature of the 410-km seismic discontinuity. *Nature*, 392, pp. 702–705.
- Ito, E. and Takahashi, E., 1989. Postspinel transformations in the system  $\text{Mg}_2\text{SiO}_4$ – $\text{Fe}_2\text{SiO}_4$  and some geophysical implications. *J. Geophys. Res.* 94, pp. 10646–10673.
- Katsura, T. and Ito, E., 1989. The system  $\text{Mg}_2\text{SiO}_4$ – $\text{Fe}_2\text{SiO}_4$  at high pressures and temperatures: precise determination of stabilities of olivine, modified spinel, and spinel. *J. Geophys. Res.* 94, pp. 15663–15670.
- Katsura, T., et al., 2003. Post-spinel transition in  $\text{Mg}_2\text{SiO}_4$  determined by high *P*–*T* in situ X-ray diffractometry. *Phys. Earth Planet. Int.* 136, pp. 11–24.
- Lebedev, S., et al., 2002a. Seismic evidence for olivine phase change at the 410- and 660-kilometer discontinuities. *Science* 296, pp. 1300–1302.
- Lebedev, S., et al., 2002b. The 660-km discontinuity within the subducting NW-Pacific lithospheric slab. *Earth Planet. Sci. Lett.* 205, pp. 25–35.

- Lebedev, S., et al., 2003. Correlation between the shear-speed structure and thickness of the mantle transition zone. *Phys. Earth Planet. Int.* 136, pp. 25–40.
- Li, X., et al., 2003. Seismic study of upper mantle and transition zone beneath hotspots. *Phys. Earth Planet. Int.* 136, pp. 79–92.
- Melbourne, T., and Helmberger, D., 1998. Fine structure of the 410-km discontinuity. *J. Geophys. Res.* 103, pp. 10,091–10,102.
- Neele, F., et al., 1997. Gross errors in upper-mantle discontinuity topography from underside reflection data. *Geophys. J. Int.* 129, pp. 194–204.
- Ringwood, A.E., 1969. Phase transformations in the mantle. *Earth Planet. Sci. Lett.* 5, pp. 401–412.
- Ringwood, A.E., 1991. Phase transformations and their bearing on the constitution and dynamics of the mantle. *Geochim. Cosmochim. Acta* 55, pp. 2083–2110.
- Rost, S., and Weber, M., 2002. The upper mantle transition zone discontinuities in the Pacific as determined by short-period array data. *Earth and Planet. Sci. Lett.*, 204, pp. 347–361.
- Shearer, P.M., Flanagan, M.P., 1999. Seismic velocity and density jumps across the 410- and 660-kilometer discontinuities. *Science* 285, pp.1545–1548.
- Shim, S.-H., et al., 2001. The post-spinel transformation in  $\text{Mg}_2\text{SiO}_4$  and its relation to the 660-km seismic discontinuity. *Nature* 411, pp. 571–574.
- Shito, A., and Shibutani, T., 2001. Upper mantle transition zone structure beneath the Philippine Sea region. *Geophys. Res. Lett.* 28, pp. 871–874.
- Simmons, N.A., and Gurrola, H., 2000. Multiple seismic discontinuities near the base of the transition zone in the Earth's mantle. *Nature* 405, pp. 559–562.
- Stixrude, L., 1997. Structure and sharpness of phase transitions and mantle discontinuities. *J. Geophys. Res.* 102, pp. 14835–14852.
- Tajima, F., and Grand, S.P., 1998. Variation of transition zone high-velocity anomalies and depression of 660 km discontinuity associated with subduction zones from the southern Kuriles to Izu-Bonin and Ryuku. *J. Geophys. Res.* 103, pp. 15,015–15,036.
- Vacher, P., et al., 1998. Computation of seismic profiles from mineral physics: the importance of the non-olivine components for explaining the 660 km depth discontinuity. *Phys. Earth Planet. Int.* 106, pp. 275–298.
- Vinnik, L.P., 1977. Detection of waves converted from *P* to *SV* in the mantle. *Phys. Earth Planet. Inter.* 15, pp. 39–45.
- Wang, P., et al., 2006. Generalized Radon transform imaging of the core mantle boundary: I—Construction of image gathers. *J. Geophys. Res.*, under review.
- Wood, B.J., 1995. The effect of  $\text{H}_2\text{O}$  on the 410-kilometer seismic discontinuity. *Science*, 268, pp. 74–76.
- Wood, B.J., Rubie, D.C., 1996. The effect of alumina on phase transformations at the

660-kilometer discontinuity from Fe-Mg partitioning experiments. *Science*, 273, pp. 1522-1524.

Xu, F., and Vidale, J.E., 2003. Survey of precursors to P'P': Fine structure of mantle discontinuities. *J. Geophys. Res.* 108(B1), doi:10.1029/2001JB000817.

Zhao, L., and Chevrot, S., 2003. SS-wave sensitivity to upper mantle structure: Implications for the mapping of transition zone discontinuity topographies. *Geophys. Res. Lett.* 30(11), doi:10.1029/2003GL017223.